ARTICLE   OPEN

Check for updates

Sleuthing out exotic quantum spin liquidity in the pyrochlore magnet $Ce_2Zr_2O_7$

Anish Bhardwaj[1,2✉], Shu Zhang[3], Han Yan[4], Roderich Moessner[5], Andriy H. Nevidomskyy [iD][4✉] and Hitesh J. Changlani [iD][1,2✉]

The search for quantum spin liquids—topological magnets with fractionalized excitations—has been a central theme in condensed matter and materials physics. Despite numerous theoretical proposals, connecting experiment with detailed theory exhibiting a robust quantum spin liquid has remained a central challenge. Here, focusing on the strongly spin-orbit coupled effective $S = 1/2$ pyrochlore magnet $Ce_2Zr_2O_7$, we analyze recent thermodynamic and neutron-scattering experiments, to identify a microscopic effective Hamiltonian through a combination of finite temperature Lanczos, Monte Carlo, and analytical spin dynamics calculations. Its parameter values suggest the existence of an exotic phase, a π-flux U(1) quantum spin liquid. Intriguingly, the octupolar nature of the moments makes them less prone to be affected by magnetic disorder, while also hiding some otherwise characteristic signatures from neutrons, making this spin liquid arguably more stable than its more conventional counterparts.

INTRODUCTION

The search for quantum spin liquids (QSL)—exotic forms of matter with fractionalized excitations—has drawn much attention of the physics community. While theories are no longer in short supply, tracking down materials has turned out to be remarkably tricky, in large part because of the difficulty to diagnose experimentally a state with only topological, rather than conventional, forms of order. Pyrochlore systems have proven a particularly promising ground, with the spin ices $Dy/Ho_2Ti_2O_7$[1] hosting a classical Coulomb phase[2–5], with subsequent proposals of candidate QSLs in other pyrochlores[6]. Quantum fluctuations have a tendency to pick an ordered state from the classically degenerate ice manifold via the "order by disorder"[7] mechanism, making QSLs extremely rare in nature. However, it is known that certain QSLs exist as a robust phase in realistic theoretical models on the pyrochlore lattice[8]; and one thus hopes that a material can be found that realizes a "quantum spin ice".

The recently discovered pyrochlore $Ce_2Zr_2O_7$[9,10] shows tremendous promise as the long sought-after QSL/quantum spin ice. Its neutron-scattering response shows a complete lack of magnetic ordering and the presence of a continuum of spectral weight[9,10], a characteristic hallmark of fractionalized excitations. Additionally, no signature of an ordering transition at low temperature has been observed in the specific heat. These observations immediately led to the proposals that $Ce_2Zr_2O_7$ might provide a realization of a QSL.

What makes the cerium-based $Ce_2Zr_2O_7$ pyrochlore distinct from the earlier studied Yb-based quantum spin-ice candidate $Yb_2Ti_2O_7$[11–14] is the dipolar-octupolar nature[15–17] of the ground state doublet of the Ce^{3+} ion, shown schematically in Fig. 1(a). It is given by the $|J = 5/2, m_J = \pm 3/2\rangle$ doublet, where the quantization axis z is chosen as the local [111] axis of the cubic lattice[9]. The transverse components of the angular momentum thus have vanishing expectation values in the ground state, which in turn implies that they are invisible to the spin-flip scattering in the neutron-scattering experiments because $\Delta m_J =$

3 excitations do not couple, to leading order, to the dipolar magnetic moment of neutrons. Using an effective pseudospin 1/2 representation of the ground state doublet[15], one of the three components (historically denoted s^y) represents the octupolar moment, and the other two components (s^x and s^z) transform as the the familiar dipole.

The key to the unusual properties of $Ce_2Zr_2O_7$ is the effective interactions between spin components, both dipolar and octupolar, belonging to the nearest-neighbors Ce ions, which are different from the thoroughly studied dipolar spin ice. A model nearest neighbor (nn) Hamiltonian incorporating all symmetry-allowed spin-spin interactions on the pyrochlore lattice is[15]:

$$H_{nn} = \sum_{\langle ij \rangle} J_y s_i^y s_j^y + [J_x s_i^x s_j^x + J_z s_i^z s_j^z + J_{xz}(s_i^x s_j^z + s_i^z s_j^x)], \tag{1}$$

with s_i again expressed in the local frame, i.e., relative to the local [111] direction on a given Ce site (for a detailed expression in the global frame see Supplementary Note 1). J_x, J_y, J_z, and J_{xz} are magnetic coupling strengths and $\langle ij \rangle$ refers to nearest neighbor pairs of sites.

While the form of the Hamiltonian is dictated by symmetry, the values of the parameters, which dictate the location of the material on a theoretical phase diagram, depend on its chemistry. Owing to the multiple competing scales, predicting these numbers accurately from first-principles calculations is known to be challenging and has been the subject of various past and ongoing debates (see for example, refs. [18,19]). The route we take is to optimize the parameters in Eq. (1) by quantitatively reproducing results of multiple experiments using a combination of quantum and classical methods. After accomplishing this objective, we appeal to known theoretical predictions and infer the kind of phase $Ce_2Zr_2O_7$ realizes. We find that all our optimized parameter sets lie in a π-flux U(1) QSL part of a previously constructed mean-field phase diagram[20].

[1]Department of Physics, Florida State University, Tallahassee, FL 32306, USA. [2]National High Magnetic Field Laboratory, Tallahassee, FL 32310, USA. [3]Department of Physics & Astronomy, University of California, Los Angeles, CA, USA. [4]Department of Physics & Astronomy, Rice University, Houston, TX 77005, USA. [5]Max Planck Institute for Physics of Complex Systems, 01187 Dresden, Germany. ✉email: ab12k@my.fsu.edu; nevidomskyy@rice.edu; hchanglani@fsu.edu
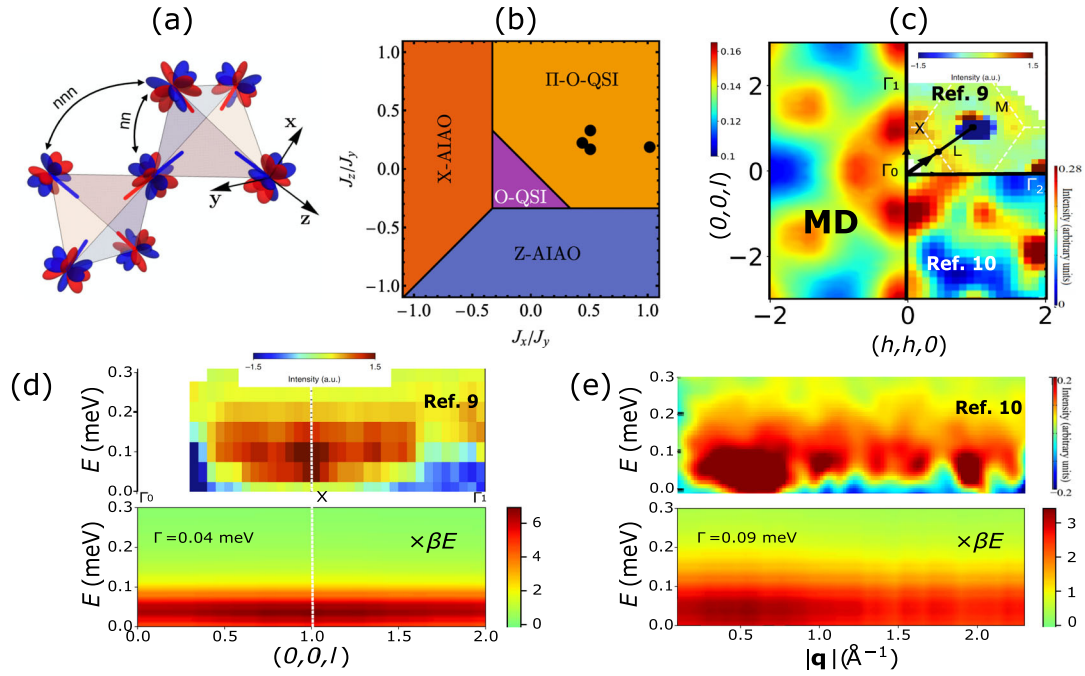
Fig. 1 Quantum spin liquid in a pyrochlore magnet and its experimental ramifications. a Depiction of a pyrochlore lattice with octupolar components forming 2-in-2-out ice states, and showing representative nearest neighbor (nn) and next-nearest neighbor (nnn) bonds. **b** Our model parameter sets are shown with black dots, superposed on the mean-field phase diagram of ref. [20]. **c** Dynamical structure factors at $T = 0.06$ K integrated over the energy range 0.00 to 0.15 meV obtained from classical molecular dynamics (MD) for 8192 spins along with the corresponding comparison with ref. [9] ($T = 0.035$ K) and ref. [10] ($T = 0.06$ K, with an additional background subtraction). The plots reported in the published references were adapted for the purpose of comparison with our results. Special points in the Brillouin zone are also shown. **d, e** The dynamical structure factor as function of energy and momentum using the MD data (for 1024 sites) compared to experiment. The quantum-classical correspondence dictates that the MD data be rescaled[23] by the factor βE ($\beta = 1/k_B T$ where k_B is the Boltzmann factor, and E is the neutron energy transfer). Panel **d** is for the momentum $(0, 0, l)$ cross section ($\Gamma_0 \rightarrow X \rightarrow \Gamma_1$) and panel **e** is the powder average. For panels **c, d, e** the numerically optimized Hamiltonian (parameter set no. 2 with both nearest neighbor and next-nearest neighbor terms, see Supplementary Table 1) was simulated. Additional Lorentzian convolution of width Γ was applied to mimic the limited experimental resolution, based on values reported in ref. [9] and ref. [10]. The color scheme used for the theoretical calculation and the two experiments differs, and in the absence of additional information only the relative variations should be compared. Note that the high intensity around $\mathbf{q} = (1, 1, \pm 1)$ and $(2, 2, -2)$ seen in the experimental inset in panel **c** results from an imperfect subtraction (using high-temperature data) of the nuclear Bragg peaks, which are absent from our theoretical calculations. The same is true in panel **e** at $|\mathbf{q}| \sim 1$ Å^{-1} and $|\mathbf{q}| \sim 2$ Å^{-1}, where the maxima of intensity originate from imperfect subtraction of nuclear Bragg peaks.

RESULTS

Effective Hamiltonian from specific heat and magnetization

By fitting the experimental magnetization and specific heat to (quantum) finite temperature Lanczos method (FTLM) calculations[21] (see Fig. 2, Methods and Supplementary Note 2 for more details), we have determined the parameters of the model Hamiltonian in Eq. (1). A crucial result from the modeling perspective is that we have identified the J_y interaction — which acts between the octupolar components — to be the largest term ($J_y \approx 0.1$ meV), with two interactions (J_x and J_z) playing a subleading role, and a vanishing J_{xz}. We have obtained several sets of parameter values (see Supplementary Table 1) within the fitting error bars, shown by the black dots in Fig. 1(b), clustered around $J_y = 0.08 \pm 0.01$ meV, $J_x = 0.05 \pm 0.02$ meV, $J_z = 0.02 \pm 0.01$ meV. We show additional cost function analyses for a wide range of J_x, J_y and J_z in Supplementary Note 3, that illustrate constraints on our fits given the current availability of experimental data. Additionally, since the fitting was performed using a 16-site cluster to reduce the computational cost, we also verified that the parameters adequately describe a 32-site system (see Supplementary Note 4).

Inelastic neutron spin structure factor

Note that since the octupolar s^y moments do not couple to neutron spins to leading order, it is crucial to perform fits to the

magnetization and specific heat as described above; attempts to fit solely the dynamical structure factors (see expressions in Supplementary Note 5) measured in inelastic neutron scattering (INS) are less reliable. We do employ the INS data, however, at the second stage of our fitting process. After determining H_{nn}, we introduce an additional weak next-nearest neighbor (nnn) coupling J_{nnn} (see Methods and Supplementary Note 1), which likely originates from the magnetic dipole-dipole interaction between Ce ions. Its optimal value $J_{nnn} \sim -0.005J_y \approx -0.5$ μeV was determined by comparing the Self-Consistent Gaussian Approximation (SCGA) prediction of the spin structure factor with INS data (see Fig. 2(c)).

Armed with this complete Hamiltonian (nn and nnn terms), we compute the energy-integrated and energy-resolved momentum-dependent neutron spin structure factor using classical Molecular Dynamics (MD)[22–24] for $N = 1024$ and $N = 8192$ sites. Representative comparisons with previous experiments on $Ce_2Zr_2O_7$[9,10] are shown in Fig. 1(c–e). Figure 1(c) shows the characteristic ring-like structure centered around $\Gamma_0 = (0, 0, 0)$ point, with pronounced maxima at $|\mathbf{q}| = 1$ (in particular $\mathbf{q} = (0, 0, 1)$ and $(\frac{1}{\sqrt{2}}, \frac{1}{\sqrt{2}}, 0)$ where we use the standard Miller indices (h, k, l) to denote the location in reciprocal space), consistent with experimental observations. Using the quantum-classical correspondence to rescale the MD data[23], in Fig. 1(d) we show the results for a one-dimensional cross section in momentum space ($\Gamma_0 \rightarrow X \equiv (0, 0, 1) \rightarrow \Gamma_1 \equiv (0, 0, 2)$). The increased intensity at
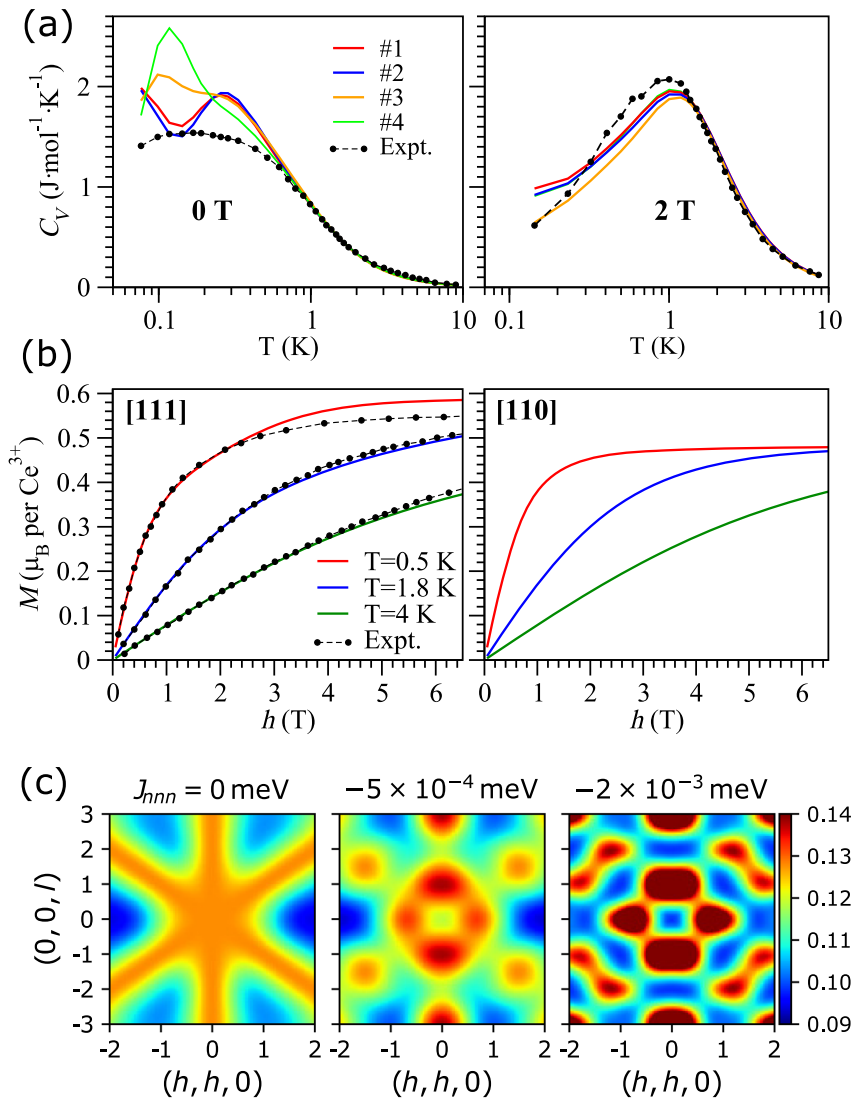
Fig. 2 Fitting magnetization, specific heat, and neutron-scattering data to obtain the model Hamiltonian parameters. Results of a two-stage fitting process used to determine the optimal Hamiltonian consistent with all reported experiments. **a** Specific heat as a function of temperature obtained for four different model parameter sets, vs. experimental data (extracted from ref. [9]) for the case of zero field and applied field of 2 T along the [111] direction. **b** Magnetization obtained from finite temperature Lanczos of the model Eq. (1) on a 16-site cluster (for analysis of finite-size effects, see Supplementary Note 4) as functions of magnetic field applied along the [111] and [110] directions. For clarity, the theoretical data is shown for one parameter set only (set no. 2, see Methods and Supplementary Note 3, also for fits with other parameter sets, of comparable quality) and only the experimental results for magnetization (extracted from ref. [9]) with field along [111] direction have been shown. **c** The predicted zero-field neutron-scattering structure factor $S(\mathbf{q})$, Eq. (4), computed with SCGA, for three different values of J_{nnn}, with the left panel ($J_{nnn} = 0$) corresponding to the nearest-neighbor only model, Eq. (1).

the X point at low energies is broadly consistent with experimental findings (additionally, see Supplementary Note 6). Figure 1(e) shows our results for the powder averaged case, compared with the experimental data in ref. [10], suggesting an overall agreement of the energy scales over the entire Brillouin zone (the X point corresponds to $|\mathbf{q}| \sim 0.6\,\text{Å}^{-1}$ in physical units, where the intensity is highest).

The fact that multiple experimental features are accurately reproduced by a model of dipolar-octupolar interactions between the Ce spin components in Eq. (1) (plus a small J_{nnn} term) poses the question about what phase corresponds to its ground state. Indeed, the fact that the coupling J_y between the nearest neighbor octupolar moments is antiferromagnetic and by far the largest suggests that the leading behavior is for the corresponding components to form a (classical) 2-in/2-out spin-ice manifold (In Supplementary Note 7, we show additional evidence for the importance of J_y in explaining the experimental data). The presence

of non-zero J_x and J_z interactions then adds quantum effects; generically, this opens the possibility of obtaining a quantum spin-ice phase.

Quantum spin-ice phase

The phase diagram for the model Hamiltonian in Eq. (1) was studied in refs. [20,25], using a combination of analytical and mean-field analysis as well as exact diagonalization. In our modeling of the magnetization and specific heat, we have determined four candidate sets of fitting parameters depicted by black dots in Fig. 1(b). All four fall deep into the parameter regime of the π-flux octupolar quantum spin-ice (π-OQSI) phase, based on the phase diagram of ref. [20]. In this phase, the emergent gauge field A takes a non-trivial ground state configuration that hosts a flux $\Phi = \pi$
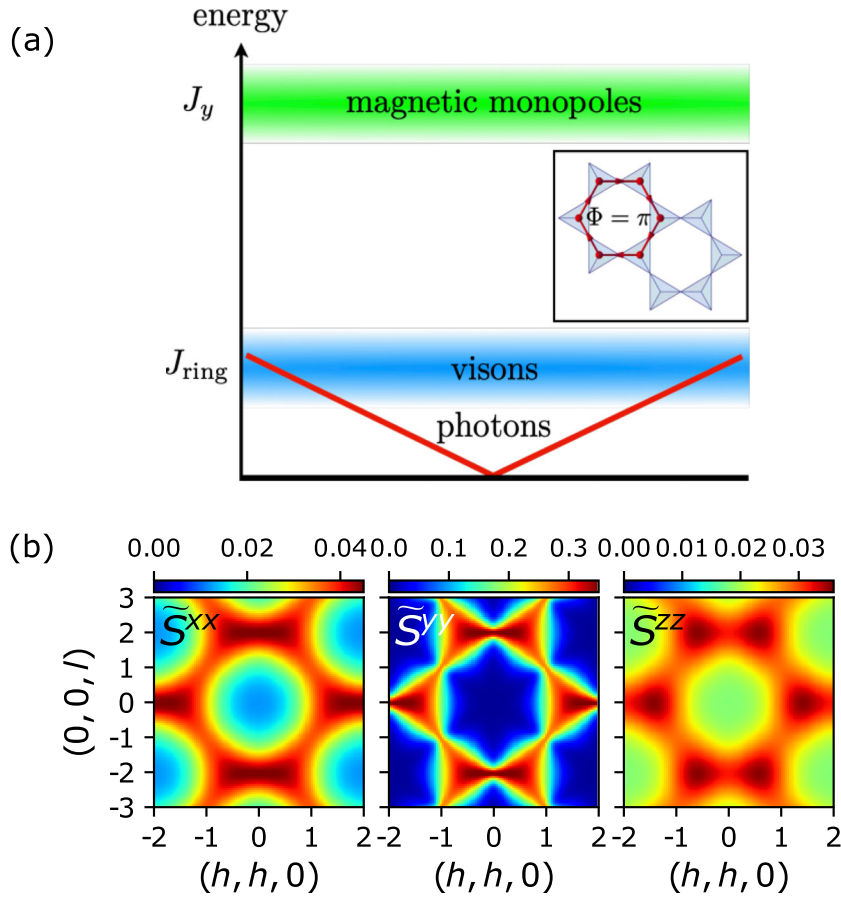
(a)

(b)

Fig. 3 Properties of the octupolar quantum spin-ice state. a Schematic depiction of the energy spectrum of π-OQSI state, with the green band denoting the spin-flip excitations that create a pair of magnetic monopoles (spinons). The blue band represents the dispersive, gapped vison excitations, which are analogous to electric charges. The red line is the hallmark of gauge-neutral photon excitations of the quantum spin-ice, except here the octupolar (rather than dipolar) character renders the photons "invisible" to neutrons. Inset, Representation of the gauge flux Φ through the hexagon formed by 6 corner-sharing tetrahedra on the pyrochlore lattice. **b** The diagonal pseudospin correlation functions $\tilde{S}^{xx}$, $\tilde{S}^{yy}$, and $\tilde{S}^{zz}$ (see $\tilde{S}^{\alpha\beta}(\mathbf{q})$ defined in the main text). Here x, y, z are the local axes (relative to the local $\hat{\mathbf{z}} = [111]$ direction). The pinch-point patterns in the $\tilde{S}^{yy}$ channel are invisible to neutrons because of the octupolar nature of s^y.

through each hexagon[26–28],

$$\nabla_{\bigcirc} \times A \equiv \sum_{i \in \bigcirc} A_{\mathbf{r}_i, \mathbf{r}_{i+1}} = \pi, \tag{2}$$

where $\mathbf{r}_i$ is the site of the dual diamond lattice, and the spins and A live on the links $\mathbf{r}_i, \mathbf{r}_{i+1}$ of the pyrochlore lattice, as shown schematically in the inset of Fig. 3(a). This fact follows from the effective U(1) quantum field theory, described in the Supplementary Note 8, with the flux-dependent contribution in the form

$$H_{\text{flux}} = J_{\text{ring}} \sum_{\bigcirc} \cos(\nabla_{\bigcirc} \times A), \tag{3}$$

where $J_{\text{ring}} \sim (J_x + J_z)^3/(64J_y^2)$ is positive and thus favors flux $\Phi = \pi$ in each hexagon, resulting in the π-OQSI phase.

Like "conventional" quantum spin ice, π-OQSI has gapless photons and two types of gapped excitations (magnetic and electric charges), in close analogy to Maxwell electrodynamics. Their approximate energy scales are illustrated in Fig. 3(a). The first type of gapped excitations are spinons created in pairs by flipping the octupolar moment on a single site, costing energy $\mathcal{O}(J_y)$. These are analogs of the magnetic monopoles in electrodynamics, and observable in the specific heat as a characteristic Schottky peak at energy $\sim J_y \approx 1$ K, as our FTLM calculations corroborate in Fig. 2(a). The second type of gapped excitations corresponds to the so-called

visons (analogs of electric charges), which are sources of the gauge flux violating the condition in Eq. (2). Note the energy scale for exciting visons at $J_{\text{ring}} \sim 0.01$ K is very low. One therefore expects to find thermally excited visons even at the base temperature of the experiment, so that their gap, if not closed by the quantum dynamics, will not be separately resolved. Rather, visons will strongly interact and mix with the emergent gapless photons, named in analogy to the photons familiar from Maxwell electrodynamics, due to the overlap of their energy scales [cf. Fig. 3(a)].

The energy and temperature scales for observing the photons would correspondingly be very low. More importantly, they would not directly couple to neutrons because of the octupolar nature of the π-OQSI. To illustrate this point, we have computed the pseudospin correlation functions $\tilde{S}^{\alpha\beta}(\mathbf{q}) = \frac{1}{N}\sum_{i,j} e^{i\mathbf{q}\cdot(\mathbf{r}_i - \mathbf{r}_j)}\langle s^\alpha(\mathbf{r}_i)s^\beta(\mathbf{r}_j)\rangle$ in Fig. 3(b) by SCGA (see Methods for details). The largest components of this matrix are the diagonal ones $\tilde{S}^{xx}$, $\tilde{S}^{yy}$ and $\tilde{S}^{zz}$. It is the octupolar $\tilde{S}^{yy}(\mathbf{q})$ component in the middle panel of Fig. 3(b) that displays the pinch-points characteristic of the spin-ice[4,29], and the photons' gapless dispersion will emanate from the $\mathbf{q}$ location of those pinch-points. Crucially however, the s^y components of spin, at leading order, do not couple to the magnetic field or to the neutron moment (see Methods, especially Eq. (6)), meaning that the aforementioned pinch-points will not feature in the experiment. Instead, the (energy-integrated)
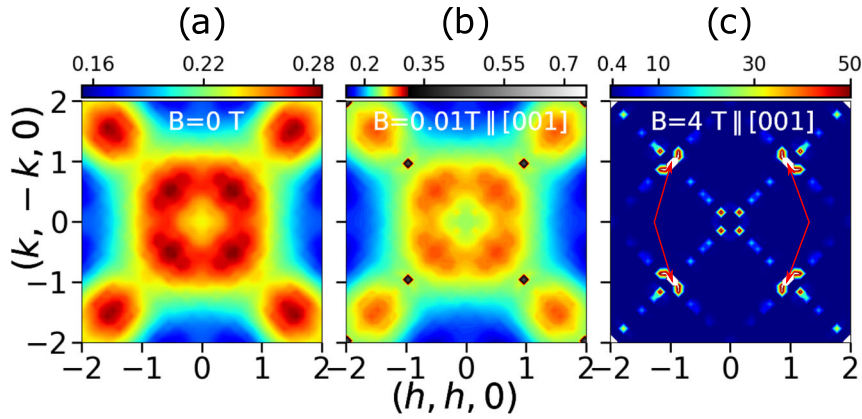
Fig. 4 Predictions for static spin structure factor as expected to be measured in INS. The predicted (energy-integrated) neutron-scattering spin structure factor (in arbitrary units) in **a** zero field and an applied magnetic field along [001] **b** $B = \mu_0 H = 0.01$ T and **c** $B = \mu_0 H = 4$ T, computed using MC calculations for 8192 sites at $T = 0.1$ K. The Bragg peaks at 4 T, which have intensity value ~3400, appear in the white regions indicated with arrows.

neutron-scattering structure factor

$$S(\mathbf{q}) = \frac{1}{N} \sum_{\mu\nu} \left(\delta_{\mu\nu} - \frac{q_\mu q_\nu}{q^2} \right) \sum_{i,j} e^{i\mathbf{q}\cdot(\mathbf{r}_i - \mathbf{r}_j)} \langle m^\mu(\mathbf{r}_i) m^\nu(\mathbf{r}_j) \rangle \quad (4)$$

is expressed in terms of true magnetic moments $m^\mu = \sum_\lambda g^{\mu\lambda} s^\lambda$ that contain the g-factors, whose $g^{\mu y}$ components are all zero (see Supplementary Note 1). As a consequence, $\tilde{s}^{yy}$ drops out of the neutron structure factor, computed in Figs. 1(c) and 2(c) using Monte Carlo and SCGA respectively. The main contributors to the neutron-scattering structure factor are the $\tilde{S}^{xx}$ and $\tilde{S}^{zz}$ channels convoluted with the neutron-coupling form factor in Eq. (4). As a result, instead of the pinch-points, a sixfold, three-rod-crossing-like pattern is observed. Such a rod pattern is expected for a pyrochlore lattice with nearest-neighbor interactions only[30] and is associated with the dispersion of spinons (magnetic monopoles) in the context of quantum spin ice[30–32].

Upon inclusion of (weak) nnn interactions J_{nnn}, the pattern of crossing rods deforms into a characteristic ring-like structure that appears in $S(\mathbf{q})$, as shown in the three panels of Fig. 2(c). Phenomenologically fixing the value $J_{nnn} \sim -0.5$ μeV matches very well with the experimental INS observations [see Fig. 1(c)]. Thence, while it is tempting to associate the intensity variation along the rods in Fig. 2(c) as the disappearance of pinch-point intensity centered at $(1, 1, 1)$ (and equivalent points), which has been predicted to be the quintessential feature of the dispersive, quantum photon modes in dipolar quantum spin ice[33], our analysis rather suggests that these are the consequence of the small nnn interactions between Ce ions that modulate the INS intensity along the [111] direction. As for the emergent photons, while they are indeed expected to be present in the π-OQSI phase, as shown in Fig. 3(a), their octupolar nature turns out to render them much less visible to neutrons, and they can only be detected via weaker, higher-order coupling to neutrons at large momentum transfer[34,35], or indirectly, for instance through their contribution to the low-temperature specific heat (at $T \lesssim J_{ring}/k_B \approx 0.01$ K).

DISCUSSION

Given the effective microscopic description of Ce$_2$Zr$_2$O$_7$, an interesting question is to ask how the (putative) octupolar quantum spin-ice state responds to the application of an external magnetic field[25]. While the octupolar s^y pseudospin components do not couple linearly to the field and will remain in the 2-in/2-out configuration, the s^z components will cant along the field direction (see Eq. (6), where $g_x \approx 0$). In order to elucidate the experimental consequences, we compute the in-field spin structure factor $S(\mathbf{q})$

within classical Monte Carlo calculations on our model for 8192 sites, shown in Fig. 4. As a function of increasing field along the [001] direction, the ring-like structure in $S(\mathbf{q})$ quickly weakens (Fig. 4b), until eventually disappearing and giving way to sharp Bragg peaks in high fields (Fig. 4c). These predictions are to be compared with future INS data in an applied magnetic field.

The fact that the magnetic octupolar degrees of freedom do not couple in the leading order to neutron spin or to the external magnetic field, makes the octupolar spin liquid difficult to detect. Its elusive nature may however prove to be a blessing in disguise, as a reduced coupling to magnetic defects and associated stray magnetic fields—which are known to destabilize the more conventional dipolar spin liquids—is similarly suppressed. Indeed, chemical disorder on magnetic sites is believed to be the leading reason for the failure to observe the quantum spin liquid behavior in, for instance, the herberthsmithite kagome compounds despite their high crystallographic quality[36]. The fact that neither magnetic order *nor* spin glassiness is seen in cerium pyrochlores Ce$_2$Zr$_2$O$_7$ and Ce$_2$Sn$_2$O$_7$[34,37] may be taken as an additional, albeit indirect, evidence of the robustness of the underlying octupolar spin liquid. While the possibility of such a quantum spin liquid has been entertained in seminal theoretical studies before[15,20], our present work firmly identifies Ce$_2$Zr$_2$O$_7$ as a very promising host for the π-flux octupolar quantum spin-ice phase. The present study also underscores the importance of carefully fitting multiple experiments, including specific heat and magnetization, in addition to the INS spectra, to determine the effective model Hamiltonian, which otherwise may be plagued with uncertainties affecting the searches and identification of QSLs[18,19].

METHODS
Fitting model Hamiltonian parameters
In addition to the nearest neighbor (nn) Hamiltonian in Eq. (1) we have considered the next-nearest neighbor (nnn) interaction, which in the local basis is given by,

$$H_{nnn} = \sum_{\langle\langle i,j \rangle\rangle} J_{nnn} \begin{bmatrix} s_i^x & s_i^y & s_i^z \end{bmatrix} \begin{bmatrix} g_x^2 & 0 & g_x g_z \\ 0 & 0 & 0 \\ g_x g_z & 0 & g_z^2 \end{bmatrix} \begin{bmatrix} s_j^x \\ s_j^y \\ s_j^z \end{bmatrix}. \quad (5)$$

where $\langle\langle i, j \rangle\rangle$ refers to nnn pairs of sites.

For the case of an applied external magnetic field, the Zeeman term must also be accounted for. This term involves the coupling of magnetic field to effective spin 1/2 degrees of freedom, which are not the usual and familiar dipoles, and are instead dipolar-octupolar doublets. A key observation is that the octupolar magnetic moments do not couple, to linear order, to the external magnetic field. The octupolar moments can in

principle couple to the third power of the magnetic field H^3 (ref. [20]), however, this effect is expected to be small for the experimentally accessible fields. It can be shown that only the component of the field H along the local z-axis couples to the dipole moment[15], as follows:

$$H_Z = -\sum_i (\mathbf{h} \cdot \mathbf{z}_i)(g_z s_i^z + g_x s_i^x), \tag{6}$$

where $|\mathbf{h}| = \mu_B \mu_0 H$ is the effective magnetic field strength, μ_B is the Bohr magneton. Note that when projected onto the $J = 5/2$ multiplet, one expects the Landé g-factor $g_z = 2.57$ and $g_x = 0$. However, if an admixture of higher spin-orbit multiplet ($J = 7/2$) is present in the ground state doublet, one generically expects a non-zero value of g_x (see Supplementary Note 9), which we allow for in our modeling.

As explained in the main text, the Hamiltonian parameters in Eq. (1) were determined using both zero and finite applied magnetic field data. For the specific heat and magnetization, we have performed quantum FTLM calculations on a 16-site cluster. Details of the general technique can be found in ref. [21] and previous application to some pyrochlore systems can be found in ref. [38]. Our convergence checks of the method (see Supplementary Note 2) suggest that the statistical errors present in the specific heat and magnetization are smaller than the line width used in Fig. 2. Figure 2(a) shows the temperature dependence of the specific heat and suggests that fitting it is somewhat challenging, both in zero and applied field. Our four distinct parameter sets are generally able to describe specific heat very well at higher temperature $T \gtrsim 1$ K, however, the lower-temperature behavior is trickier and none of the parameter sets used satisfactorily fit the data especially in the absence of applied magnetic field. We attribute this to the finite-size effects in our FTLM calculations, which become more pronounced at lower temperatures. The magnetization as a function of applied field strength, shown in Fig. 2(b), appears to be less prone to finite-size effects (also see Supplementary Note 4) and is fitted reasonably well, especially at low fields. The discrepancy at high fields is not entirely unexpected, previous experimental reports have suggested a changing g-factor past a $\mu_0 H = 4$ T field[9], an effect not built into our model.

Despite the finite-system size limitations of the numerical calculations, and the finite energy and momentum resolution in INS experiment, all our parameter sets obtained are in agreement with J_y being antiferromagnetic. For three of these sets, we find J_y is large compared to the other two interactions (J_x and J_z) in Eq. (1), as depicted in Fig. 1(b) (also see Supplementary Note 7). A fourth parameter set, obtained by constraining g_x to be zero, suggests $J_y \approx J_x > J_z$. To further build confidence in our results, we have performed a brute force scan of J_x and J_z for representative fixed values of J_y and constructed a contour map of an appropriately defined cost function (see Supplementary Note 3, more subtleties with the fitting and additional competitive parameter sets are also discussed). Additional future experiments could potentially further constrain the values of these coupling constants.

The second step of our parameter fitting involved the determination of J_{nnn}, which we found to be small relative to J_y. Despite its smallness, it is responsible for significant reorganization of intensity in the Brillouin zone. Figure 2(c) shows the static structure factor in the (h, h, l) plane computed with SCGA (the details of which will be explained shortly) for representative values of J_{nnn}. Performing a brute force line search, we determined the optimal value $J_{nnn} = -5 \times 10^{-4}$ meV working in steps of 10^{-4} meV.

The following values of the parameters (which we refer to as set no. 2, see Supplementary Note 3) were used in subsequent calculations (all values are in meV): $J_x = 0.0385, J_y = 0.088, J_z = 0.020, J_{xz} = 0, J_{nnn} = -0.0005$, with the g-factors $g_x = -0.2324, g_z = 2.35$. The other parameters sets are quoted in full in the Supplementary Table 1.

Details of the Monte Carlo and molecular (spin) dynamics calculations

For the Hamiltonian $\mathcal{H} \equiv H_{nn} + H_{nnn} + H_Z$, the dynamical structure factor is computed by integrating the classical Landau–Lifshitz equations of motion

$$\frac{d}{dt}\mathbf{S}_i = -\mathbf{S}_i \times \frac{\partial \mathcal{H}}{\partial \mathbf{S}_i}, \tag{7}$$

which describes the precession of the spin in the local exchange field. We carry out all our calculations by transforming our Hamiltonian to the global basis, and have used the label $\mathbf{S}_i$ to represent spins in this basis (see Supplementary Note 1 for more details on transformations between local and global bases).

Following the protocol adopted in previous work[22,23], the initial configuration (IC) of spins is drawn by a Monte Carlo (MC) run from the Boltzmann distribution $\exp(-\beta \mathcal{H})$ at temperature $T = \beta^{-1} = 0.06$ K. Then, for each starting configuration the spins are deterministically evolved according to Eq. (7) with the fourth order Runge-Kutta method. This procedure, referred to as molecular dynamics (MD) (also see Supplementary Note 5), is repeated for many independent IC (their total number being N_{IC}) and the result is averaged,

$$\langle S_i^\mu(t) S_j^\nu(0) \rangle = \frac{\sum_{IC \text{ from } MC} S_i^\mu(t) S_j^\nu(0)|_{IC}}{N_{IC}}. \tag{8}$$

We perform a Fourier transform in spatial and time coordinates to get the desired dynamical structure factor. We work with $N = 16L^3$ sites, where L^3 is the number of cubic unit cells, the results in Fig. 1(c) are for $L = 8$ ($N = 8192$) and $L = 4$ ($N = 1024$) for Fig. 1(d, e). $N_{IC} \approx 10^4$ was used, and each IC was evolved for 500 meV^{-1} in steps of $\delta t = 0.02$ meV^{-1}. The statistical error bars in the classical MD/MC simulations presented are small enough to not change the features of the color plots.

To obtain an estimate of the quantum dynamical structure factor, we used a classical-quantum correspondence, which translates to a simple rescaling of the classical MD data by βE. More details and justification can be found in ref. [23].

Convolution with Lorentzian function to mimic limitations of experimental resolution

Figure 1(d, e) shows significant broadening along the energy axis, an effect not captured to the same extent by the raw (rescaled) MD data. Since the interaction energy scales in the material are small, a fairer comparison between experiment and theory is achieved by modeling the instrument's energy resolution. Using Γ values in the ballpark suggested by refs. [9,10], we convolved our data with a Lorentzian factor,

$$S_{exp}(\mathbf{q}, E) = \frac{1}{\pi} \int S(\mathbf{q}, E')_{MD} \frac{\Gamma}{\Gamma^2 + (E' - E)^2} dE' \tag{9}$$

The integral was approximated by a sum over discrete E' points in steps of 0.01 meV.

Details of the SCGA calculations

The Self-Consistent Gaussian Approximation is an analytical method that treats the spin in the Large-N (flavor) limit. Our calculation follows closely ref. [4]. In this study, we first treat $s^{x,y,z}$ as independent, freely fluctuating degrees of freedom. The Hamiltonian in momentum space is written as

$$\mathcal{E}_{Large-N} = \frac{1}{2}\mathbf{S}\mathcal{H}_{Large-N}\mathbf{S}^T, \tag{10}$$

where $\mathbf{S} = (s_1^x, s_2^x, s_3^x, s_4^x, \dots, s_3^z, s_4^z)$. The interaction matrix $H_{Large-N}$ is the Fourier transformed interaction matrix that includes the nearest and next-nearest neighbor interactions.

We then introduce a Lagrangian multiplier with coefficient μ to the partition function to get

$$\mathcal{Z} = \exp\left(-\frac{1}{2}\int_{BZ}d\mathbf{k}\, d\mathbf{S}\, \mathbf{S}\left[\beta\mathcal{H}_{Large-N} + \mu\mathcal{I}\right]\mathbf{S}^T\right) \tag{11}$$

in order to impose an additional constraint of averaged spin-norm being one, or

$$\langle \mathbf{s}_1^2 + \mathbf{s}_2^2 + \mathbf{s}_3^2 + \mathbf{s}_4^2 \rangle = 1. \tag{12}$$

For a given temperature $k_B T = 1/\beta$, the value of μ is fixed by this constraint via relation

$$\int_{BZ} d\mathbf{k} \sum_{i=1}^{12} \frac{1}{\lambda_i(\mathbf{k}) + \mu} = \langle \mathbf{s}_1^2 + \mathbf{s}_2^2 + \mathbf{s}_3^2 + \mathbf{s}_4^2 \rangle = 1, \tag{13}$$

where $\lambda_i(\mathbf{k}), i = 1, 2, \dots, 12$ are the twelve eigenvalues of $\beta\mathcal{H}_{Large-N}$. With μ fixed, the partition function is completely determined for a free theory of $\mathbf{S}$, and all correlation functions can be computed from $\left[\beta\mathcal{H}_{Large-N} + \mu\mathcal{I}\right]^{-1}$.

DATA AVAILABILITY

The data analyzed in the present study is available from the first author (A.B.) upon reasonable request.

CODE AVAILABILITY

The codes used for the simulations reported in this paper are publicly available at elink https://github.com/hiteshjc/FittingwithFTLM and elink https://github.com/hiteshjc/DipoleOctupoleMD. Additional scripts and files are available from the first author (A.B.) upon request.

REFERENCES

1. Bramwell, S. T. & Gingras, M. J. P. Spin ice state in frustrated magnetic pyrochlore materials. *Science* **294**, 1495–1501 (2001).
2. Fennell, T. et al. Magnetic coulomb phase in the spin ice $Ho_2Ti_2O_7$. *Science* **326**, 415–417 (2009).
3. Morris, D. J. P. et al. Dirac strings and magnetic monopoles in the spin ice $Dy_2Ti_2O_7$. *Science* **326**, 411–414 (2009).
4. Isakov, S. V., Gregor, K., Moessner, R. & Sondhi, S. L. Dipolar spin correlations in classical pyrochlore magnets. *Phys. Rev. Lett.* **93**, 167204 (2004).
5. Henley, C. L. The 'Coulomb Phase' in frustrated systems. *Annu. Rev. Condens. Matter Phys.* **1**, 179–210 (2010).
6. Gingras, M. J. P. & McClarty, P. A. Quantum spin ice: a search for gapless quantum spin liquids in pyrochlore magnets. *Rep. Prog. Phys.* **77**, 056501 (2014).
7. Henley, C. L. Ordering due to disorder in a frustrated vector antiferromagnet. *Phys. Rev. Lett.* **62**, 2056–2059 (1989).
8. Hermele, M., Fisher, M. P. A. & Balents, L. Pyrochlore photons: The U(1) spin liquid in a $S = 1/2$ three-dimensional frustrated magnet. *Phys. Rev. B.* **69**, 064404 (2004).
9. Gao, B. et al. Experimental signatures of a three-dimensional quantum spin liquid in effective spin-1/2 $Ce_2Zr_2O_7$ pyrochlore. *Nat. Phys.* **15**, 1052–1057 (2019).
10. Gaudet, J. et al. Quantum spin ice dynamics in the dipole-octupole pyrochlore magnet $Ce_2Zr_2O_7$. *Phys. Rev. Lett.* **122**, 187201 (2019).
11. Ross, K. A., Savary, L., Gaulin, B. D. & Balents, L. Quantum excitations in quantum spin ice. *Phys. Rev. X* **1**, 021002 (2011).
12. Scheie, A. et al. Multiphase magnetism in $Yb_2Ti_2O_7$. *Proc. Natl Acad. Sci. USA* **117**, 27245–27254 (2020).
13. Scheie, A. et al. Reentrant phase diagram of $Yb_2Ti_2O_7$ in a $\langle 111 \rangle$ magnetic field. *Phys. Rev. Lett.* **119**, 127201 (2017).
14. Applegate, R. et al. Vindication of $Yb_2Ti_2O_7$ as a model exchange quantum spin ice. *Phys. Rev. Lett.* **109**, 097205 (2012).
15. Huang, Y.-P., Chen, G. & Hermele, M. Quantum spin ices and topological phases from dipolar-octupolar doublets on the pyrochlore lattice. *Phys. Rev. Lett.* **112**, 167203 (2014).
16. Li, Y.-D & Chen, G. Symmetry enriched U(1) topological orders for dipole-octupole doublets on a pyrochlore lattice. *Phys. Rev. B* **95**, 041106 (2017).
17. Yao, X.-P., Li, Y.-D. & Chen, G. Pyrochlore U(1) spin liquid of mixed-symmetry enrichments in magnetic fields. *Phys. Rev. Res.* **2**, 013334 (2020).
18. Laurell, P. & Okamoto, S. Dynamical and thermal magnetic properties of the Kitaev spin liquid candidate α-$RuCl_3$. *NPJ Quant. Mater.* **5**, 2 (2020).
19. Maksimov, P. A. & Chernyshev, A. L. Rethinking $\alpha - RuCl_3$. *Phys. Rev. Res.* **2**, 033011 (2020).
20. Patri, A. S., Hosoi, M. & Kim, Y. B. Distinguishing dipolar and octupolar quantum spin ices using contrasting magnetostriction signatures. *Phys. Rev. Res.* **2**, 023253 (2020).
21. Avella, A. & Mancini, F. (eds.) *Strongly Correlated Systems: Numerical Methods Springer Series in Solid-state Sciences* (Springer Berlin Heidelberg, 2013).
22. Conlon, P. H. & Chalker, J. T. Spin dynamics in pyrochlore Heisenberg antiferromagnets. *Phys. Rev. Lett.* **102**, 237206 (2009).
23. Zhang, S., Changlani, H. J., Plumb, K. W., Tchernyshyov, O. & Moessner, R. Dynamical structure factor of the three-dimensional quantum spin liquid candidate $NaCaNi_2F_7$. *Phys. Rev. Lett.* **122**, 167203 (2019).
24. Samarakoon, A. M. et al. Comprehensive study of the dynamics of a classical Kitaev spin liquid. *Phys. Rev. B* **96**, 134408 (2017).
25. Placke, B., Moessner, R. & Benton, O. Hierarchy of energy scales and field-tunable order by disorder in dipolar-octupolar pyrochlores. *Phys. Rev. B* **102**, 245102 (2020).
26. Lee, S., Onoda, S. & Balents, L. Generic quantum spin ice. *Phys. Rev. B* **86**, 104412 (2012).
27. Chen, G. Spectral periodicity of the spinon continuum in quantum spin ice. *Phys. Rev. B* **96**, 085136 (2017).
28. Benton, O., Jaubert, L. D. C., Singh, R. R. P., Oitmaa, J. & Shannon, N. Quantum spin ice with frustrated transverse exchange: from a π-flux phase to a nematic quantum spin liquid. *Phys. Rev. Lett.* **121**, 067201 (2018).
29. Moessner, R. & Chalker, J. T. Low-temperature properties of classical geometrically frustrated antiferromagnets. *Phys. Rev. B* **58**, 12049–12062 (1998).
30. Castelnovo, C. & Moessner, R. Rod motifs in neutron scattering in spin ice. *Phys. Rev. B* **99**, 121102 (2019).
31. Sibille, R. et al. Experimental signatures of emergent quantum electrodynamics in Pr2Hf2O7. *Nat. Phys.* **14**, 711–715 (2018).
32. Kato, Y. & Onoda, S. Numerical evidence of quantum melting of spin ice: quantum-to-classical crossover. *Phys. Rev. Lett.* **115**, 077202 (2015).
33. Benton, O., Sikora, O. & Shannon, N. Seeing the light: experimental signatures of emergent electromagnetism in a quantum spin ice. *Phys. Rev. B* **86**, 075154 (2012).
34. Sibille, R. et al. A quantum liquid of magnetic octupoles on the pyrochlore lattice. *Nat. Phys.* **16** https://doi.org/10.1038/s41567-020-0827-7 (2020).
35. Lovesey, S. W. & van der Laan, G. Magnetic multipoles and correlation shortage in the pyrochlore cerium stannate $Ce_2Sn_2O_7$. *Phys. Rev. B* **101**, 144419 (2020).
36. Norman, M. R. Colloquium: Herbertsmithite and the search for the quantum spin liquid. *Rev. Mod. Phys.* **88**, 041002 (2016).
37. Sibille, R. et al. Candidate quantum spin liquid in the Ce^{3+} pyrochlore stannate $Ce_2Sn_2O_7$. *Phys. Rev. Lett.* **115**, 097202 (2015).
38. Changlani, H. Quantum versus classical effects at zero and finite temperature in the quantum pyrochlore $Yb_2Ti_2O_7$. Preprint at https://arxiv.org/abs/1710.02234v2 (2017).

AUTHOR CONTRIBUTIONS

A.H.N. and R.M. conceived the theoretical ideas behind the project and planned the research. A.B., S.Z., and H.J.C. conceived and carried out the analysis of the experimental data and extraction of the effective Hamiltonian, as detailed in the Methods section and in the Supplementary Materials. A.B. and H.J.C. performed the finite temperature Lanczos, classical Monte Carlo and molecular (Landau–Lifshitz) spin dynamics calculations. S.Z. and H.Y. performed the self-consistent Gaussian calculations. All authors contributed to discussion and interpretation of the results. A.B., S.Z., H.Y., and H.J.C. prepared the figures. A.H.N. and R.M. wrote the manuscript with contributions from all authors.

COMPETING INTERESTS

The authors declare no competing interests.

ADDITIONAL INFORMATION

Supplementary information The online version contains supplementary material available at https://doi.org/10.1038/s41535-022-00458-2.

Correspondence and requests for materials should be addressed to Anish Bhardwaj, Andriy H. Nevidomskyy or Hitesh J. Changlani.

Reprints and permission information is available at http://www.nature.com/reprints

Publisher's note Springer Nature remains neutral with regard to jurisdictional claims in published maps and institutional affiliations.